**RAA 2014** Vol. **14** No. **6**, 625–634 doi: 10.1088/1674–4527/14/6/002
*http://www.raa-journal.org* *http://www.iop.org/journals/raa*

***R**esearch in*
***A**stronomy and*
***A**strophysics*

# Probing the CMB cold spot through local Minkowski functionals *

Wen Zhao

Key Laboratory for Researches in Galaxies and Cosmology, Department of Astronomy, University of Science and Technology of China, Hefei 230026, China; *wzhao7@ustc.edu.cn*

Received 2013 December 27; accepted 2014 January 14

**Abstract** Both the Wilkinson Microwave Anisotropy Probe (WMAP) and Planck missions have reported an extremely cold spot (CS) centered at Galactic coordinate ($l = 209^\circ$, $b = -57^\circ$) in the cosmic microwave background map. We study the local non-Gaussianity of the CS by defining local Minkowski functionals. We find that the third Minkowski functional $\nu_2$ is quite sensitive to the non-Gaussianity caused by the CS. Compared with random Gaussian simulations, the WMAP CS deviates from Gaussianity at more than a $99\%$ confidence level with a scale of $R \sim 10^\circ$. Meanwhile, we find that cosmic texture provides an excellent explanation for these anomalies related to the WMAP CS, which could be further tested by future polarization data.

**Key words:** cosmology: cosmic microwave background

## 1 INTRODUCTION

Soon after the release of observations from NASA's Wilkinson Microwave Anisotropy Probe (WMAP) satellite on the cosmic microwave background (CMB) temperature and polarization anisotropies, some anomalies in the CMB field have been reported, including the low quadrupole, an alignment of the quadrupole and octupole, the lack of a large-scale correlation, the CMB parity asymmetry and so on (see Bennett et al. 2011 for a review). Meanwhile, nearly all the anomalies have been confirmed by recently released *Planck* data (Planck Collaboration et al. 2013), and have attracted much attention. These anomalies may imply there are some unsolved systematical errors, contaminations in the CMB observations or new physics in the early Universe.

The non-Gaussian cold spot (CS) in the CMB temperature anisotropy field was first reported in Vielva et al. (2004), and confirmed by many authors (Cruz et al. 2007a, 2005; Cayón et al. 2005; Naselsky et al. 2010; Zhang & Huterer 2010; Vielva 2010). The CMB CS is centered at Galactic coordinate ($l = 209^\circ$, $b = -57^\circ$) and has a characteristic scale of about $10^\circ$. The temperature of the CS is nearly $4\sigma$ colder than the average CMB temperature, which is independent of different detectors or different frequency channels on the WMAP satellite (Vielva et al. 2004; Cruz et al. 2005). Although physics related to the CMB CS remains mysterious, various alternative explanations for this CS have been proposed, such as the possible Sunyaev-Zeldovich effect (Cruz et al. 2008), a supervoid in the Universe (Inoue & Silk 2006, 2007; Inoue 2012), possible foregrounds or systematics (Cruz et al. 2006) or the cosmological origin (Cruz et al. 2007b, 2008). Due to the fact that nearly all

* Supported by the National Natural Science Foundation of China.

the explanations of the CS are related to local characteristics in the CMB field, studies on the local properties of the CS are necessary. In previous work (Zhao 2013), we have studied local departures of the WMAP CS from Gaussianity by the temperature in terms of its mean, variance, skewness and kurtosis. We found excesses in the local variance and skewness at large scales with $R > 5^\circ$, which imply that the WMAP CS is a large-scale non-Gaussian structure, rather than a combination of some small structures. In this paper, we shall focus on the same topic by using different local statistics. We introduce the local Minkowski functionals (MFs), and apply them to WMAP data, in particular the WMAP CS. Comparing with random Gaussian simulations, we find that for statistics based on MF $\nu_2$, the WMAP CS significantly deviates from Gaussianity at a large scale, especially at the scale $R \sim 10^\circ$. Meanwhile, similar to Zhao (2013), we find that these local non-Gaussianities in the WMAP CS can be excellently explained by a cosmic texture. If we subtract this texture from WMAP data, we find that all these anomalies associated with MFs disappear. So, our local analysis of the CS in this paper also strongly supports the cosmic texture explanation.

The outline of this paper is as follows. In Section 2, we introduce the WMAP data, which will be used in the analysis. In Section 3, we define the local MFs and apply them to WMAP data. In Section 4, we summarize the main results of this paper.

## 2 THE CMB DATA

In our analysis, we shall use the WMAP data including the NILC5 map and the 7-year WMAP internal linear combination (ILC7) map, which have the same resolution parameter $N_{\rm side} = 512$. The ILC7 map is constructed by smoothing all five WMAP frequency-band maps to a common resolution of one degree, and then combining them by the inverse of their noise level. Based on the 5-year WMAP data, in Delabrouille et al. (2009) the authors constructed a higher resolution CMB internal linear combination map, i.e. "NILC5" map, which is an implementation of a constrained linear combination of WMAP channels with minimum error variance on a frame of spheres called needlets.

The same as in previous work (Zhao 2013), in order to simulate the NILC5 map, the effective noise level and effective beam window function given in Delabrouille et al. (2009) are adopted, but for the ILC7 simulations, we ignore all noises and smooth the simulated map to a resolution of one degree. In all the random Gaussian simulations, we assume that the temperature fluctuations and noises follow a Gaussian distribution, and do not consider any effect due to the residual foreground contaminations. Throughout this paper, we assume a $\Lambda$CDM Universe with background parameters (Komatsu et al. 2011) $100\,\Omega_{\rm b}h^2 = 2.255$, $\Omega_{\rm c}h^2 = 0.1126$, $\Omega_\Lambda = 0.725$, $\tau = 0.088$, $\Delta^2_{\mathcal{R}}(k_0) = 2.430 \times 10^{-9}$ and $n_{\rm s} = 0.968$ at $k_0 = 0.002\ {\rm Mpc}^{-1}$.

## 3 APPLYING LOCAL MINKOWSKI FUNCTIONALS TO WMAP DATA

### 3.1 Minkowski Functionals

MFs characterize the morphological properties of convex, compact sets in an $n$-dimensional space. On the 2-dimensional spherical surface $\mathbb{S}^2$, any morphological property can be expanded as a linear combination of three MFs, which represent the area, circumference and integrated geodesic curvature of an excursion set (Schmalzing & Gorski 1998). For a given threshold $\nu$, it is convenient to define the excursion set $Q_\nu$ and its boundary $\partial Q_\nu$ of a smooth scalar field $u$ as follows: $Q_\nu = \{x \in \mathbb{S}^2 | u(x) > \nu\}$ and $\partial Q_\nu = \{x \in \mathbb{S}^2 | u(x) = \nu\}$. Then, the MFs $v_0$, $v_1$ and $v_2$ can be written as (Schmalzing & Gorski 1998),

$$v_0(\nu) := \int_{Q_\nu} \frac{{\rm d}a}{4\pi},\ v_1 := \int_{\partial Q_\nu} \frac{{\rm d}\ell}{16\pi},\ v_2 := \int_{\partial Q_\nu} \frac{{\rm d}\ell\,\kappa}{8\pi^2}, \tag{1}$$

where $\mathrm{d}a$ and $\mathrm{d}\ell$ denote the surface element of $\mathbb{S}^2$ and the line element along $\partial Q_\nu$, respectively, and $\kappa$ is the geodesic curvature. Given a pixelated map with field $u(x_i)$, these MFs can be numerically calculated by the formulae (Schmalzing & Gorski 1998; Lim & Simon 2012)

$$v_i(\nu) = \frac{1}{N_{\mathrm{pix}}} \sum_{k=1}^{N_{\mathrm{pix}}} \mathcal{I}_i(\nu, x_k), \quad (i = 0, 1, 2), \tag{2}$$

where

$$\begin{aligned} \mathcal{I}_0(\nu, x_k) &:= \Theta(u - \nu), \\ \mathcal{I}_1(\nu, x_k) &:= \frac{\delta(u-\nu)}{4}\mathcal{U}_1(x_k), \\ \mathcal{I}_2(\nu, x_k) &:= \frac{\delta(u-\nu)}{2\pi}\mathcal{U}_2(x_k), \\ \mathcal{U}_1(x_k) &:= \sqrt{u_{;\theta}^2 + u_{;\phi}^2}, \\ \mathcal{U}_2(x_k) &:= \frac{2u_{;\theta}u_{;\phi}u_{;\theta\phi} - u_{;\theta}^2 u_{;\phi\phi} - u_{;\phi}^2 u_{;\theta\theta}}{u_{;\theta}^2 + u_{;\phi}^2}. \end{aligned} \tag{3}$$

Note that $u_{;i}$ denotes the covariant differentiation of $u$ with respect to coordinate $i$. The delta function in these formulae can be numerically approximated through a discretization of threshold space in bins of width $\Delta\nu$ by the Heaviside step function $\delta_N(x) = (\Delta\nu)^{-1}[\Theta(x + \Delta\nu/2) - \Theta(x - \Delta\nu/2)]$. The expectation values of three MFs for a Gaussian random field are also derived in Tomita (1986), which have been explicitly expressed in equations (14) and (15) in Schmalzing & Gorski (1998).

These MFs have been applied by cosmologists to look for deviations from Gaussianity in the perturbations of the CMB (Winitzki & Kosowsky 1998; Schmalzing & Gorski 1998; Novikov et al. 1999; Eriksen et al. 2004; Hikage et al. 2006, 2008, 2009; Hikage & Matsubara 2012; Komatsu et al. 2009; Matsubara 2010). In particular in Lim & Simon (2012), the authors used the MFs to probe the cold/hot disk-like structure in the CMB. However, they found these statistics are dominated by noise for the WMAP CS. For a single WMAP or map with the resolution of *Planck*, the method can only detect the highly prominent disk, i.e. an extremely cold or hot disk with a rather large area. These can be easily understood as follows: since the MFs are constructed on the global sky, the local non-Gaussianity of the cold/hot spot over a relatively small scale has been so diluted that it is too small to detect.

### 3.2 Local Minkowski Functionals

To study the local properties of the WMAP CS, similar to previous works (Bernui & Rebouças 2009, 2010, 2012; Zhao 2013), in this paper we will define the local MFs in terms of statistics describing the CMB field. For a given full-sky WMAP data with $N_{\mathrm{side}} = 512$ (ILC7 or NILC5), we smooth them using a Gaussian filter with a smoothing scale of $\theta_{\mathrm{s}}$, since MFs are sensitive to the smoothing scale of a density field and therefore we can obtain a variety of information from density fields by using different smoothing levels. In this paper, we focus on both ILC fields smoothed by six different smoothing scales: $10'$, $20'$, $30'$, $40'$, $50'$ and $60'$. Then, we can construct the corresponding full-sky maps, $\mathcal{U}_1(x_k)$ and $\mathcal{U}_2(x_k)$, defined in Equation (3), where $u$ is the corresponding ILC temperature anisotropy map.

Now, we can define the local MFs. Let $\Omega(\theta_j, \phi_j; R)$ be a spherical cap with aperture spanning $R$ degrees, centered at $(\theta_j, \phi_j)$. The local MFs $v_i(\nu)$ $(i = 0, 1, 2)$ in this cap can be calculated by using Equation (2), which are denoted as $v_i^j(\nu; R)$ in the rest of this paper. However, here the summation is only carried out for pixels inside the cap $\Omega(\theta_j, \phi_j; R)$. Note that in our calculation, the binning range of threshold $\nu$ is set to be –3.0 to 3.0 with 24 equally spaced bins of $\nu/\sigma$ ($\sigma$ is the standard deviation of the $u$-field in this cap) per each MF. In order to quantify the same kind of MFs by a single quantity, following Hikage et al. (2009), for each $i$ (the type of MF) and $\{j, R\}$ (the cap) we can define the associated $\chi^2$ as follows

$$\chi^2 = \sum_{\alpha\alpha'} \Big[v_i^j(\nu_\alpha; R) - v_i^{\rm th}(\nu_\alpha; R)\Big] \Sigma^{-1}_{\alpha\alpha'} \times \Big[v_i^j(\nu_{\alpha'}; R) - v_i^{\rm th}(\nu_{\alpha'}; R)\Big], \tag{4}$$

where $\alpha$ and $\alpha'$ denote the number of threshold values used for binning. $v_i^{\rm th}(\nu; R)$ is the theoretical value of $v_i^j(\nu; R)$, which is independent of the superscript $j$. $\Sigma$ is the corresponding covariance matrix. Although in principle the theoretical values $v_i^{\rm th}(\nu; R)$ for the random Gaussian field can be calculated by the analytical formulae (Tomita 1986; Schmalzing & Gorski 1998), there are systematical differences compared with numerical results from the threshold used for binning, the effect of pixelization, a survey mask or other numerical artifacts (Lim & Simon 2012). To avoid this problem, in general, one should replace theoretical value $v_i^{\rm th}(\nu; R)$ by the quantity $\langle v_i(\nu; R)\rangle$ (Schmalzing & Gorski 1998; Hikage et al. 2009; Lim & Simon 2012), where $\langle v_i(\nu; R)\rangle$ is the ensemble average of the random simulations. Fortunately, in our case, the local Minkowski functionals are defined around some single pixel $j$. Thus, the values of $v_i^j(\nu; R)$ with different $j$ indices are equivalent to the quantity $v_i^j(\nu; R)$ (for the fixed $j$) in different simulations. So in this paper, we replace the theoretical value $v_i^{\rm th}(\nu; R)$ by the quantity $\langle v_i(\nu; R)\rangle$, which is the average value of all $v_i^j(\nu; R)$ with $|b_j| > 30°$. The covariance matrix $\Sigma$ can also be numerically calculated by these quantities $v_i^j(\nu; R)$ as follows

$$\Sigma_{\alpha\alpha'} = \frac{1}{n_j} \sum_j \Big[v_i^j(\nu_\alpha; R) - \langle v_i(\nu_\alpha; R)\rangle\Big] \Big[v_i^j(\nu_{\alpha'}; R) - \langle v_i(\nu_{\alpha'}; R)\rangle\Big], \tag{5}$$

where $n_j$ is the number of pixels in the region $|b_j| > 30°$, and the summation is also only carried out for the same region. Here, we should emphasize that, in the ILC7 and NILC5 maps, nearly all residuals from various contaminations are around the Galactic plane with $b \sim 0°$. In order to remove the effect of these contaminations, in our calculation for the quantities $\chi^2$, $\langle v_i(\nu; R)\rangle$ and $\Sigma_{\alpha\alpha'}$, the Galactic plane with $|b_j| < 30°$ has been masked.[1] Hereafter, we denote this $\chi^2$ quantity as $X_i^j(R)$. Clearly, the values $X_i^j(R)$ obtained in this way for each cap can be viewed as a measure of non-Gaussianity in the direction of the center of the cap $(\theta_j, \phi_j)$. For a given aperture $R$, we scan the celestial sphere with evenly distributed spherical caps, and build the $X_0(R)$-, $X_1(R)$- and $X_2(R)$-maps. In our analysis, we have chosen the locations of centroids of spots to be the pixels at a resolution of $N_{\rm side} = 64$. By choosing different $R$ values, one can study the local properties of the CMB field at different scales.

The same as the $V(R)$-map (or $S(R)$-, $K(R)$-maps) defined in Zhao (2013), here we also find that $X_i^j(R)$ is always maximized at the edge of the circles, rather than at the center of the circles. To overcome this problem and localize the non-Gaussian sources, we define the average quantities

$$\bar{X}_i^j(R) := \frac{1}{N_{\rm pix}} \sum_{j=1}^{N_{\rm pix}} X_i^j(R), \qquad (i = 0, 1, 2), \tag{6}$$

where $N_{\rm pix}$ is again the number of pixels in the $j^{\rm th}$ cap.

[1] Note that, for the WMAP V-band or W-band maps, we always have to apply complicated masks (such as the KQ75y7 mask) to exclude various contaminations caused by effects of foreground and dust. Thus, there is no way to define the quantity $\langle v_i(\nu; R)\rangle$, and the related quantity $\chi^2$ defined in Equation (4). This is the reason why we cannot apply this method to the WMAP V-band or W-band maps.

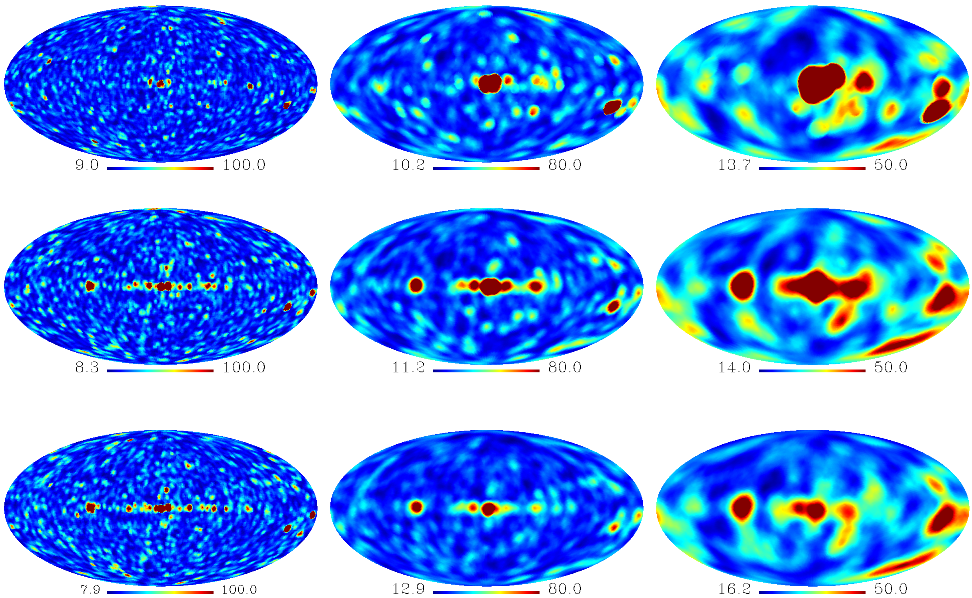


**Fig. 1** $\bar{X}_0(R)$ maps (*upper*), $\bar{X}_1(R)$ maps (*middle*) and $\bar{X}_2(R)$ maps (*lower*) for ILC7 data with $\theta_{\rm s} = 60'$ smoothing. In the left panels, we have used $R = 2°$, in the middle panels $R = 5°$ is chosen and in the right panels $R = 10°$.

We apply this method to the ILC7 data by choosing $R = 2°$ and $\theta_{\rm s} = 60'$. The $\bar{X}_i$ maps are presented in Figure 1 (left panels), which clearly show that these local statistics, in particular the third MF $v_2$, are very sensitive to the foreground residuals and various point sources. The Galactic plane is clearly presented, which is the non-Gaussian area caused by the foreground residuals in the ILC7 map. In addition, two important point sources at ($l = 209.5°$, $b = -20.1°$) and ($l = 184.9°$, $b = -5.98°$), as well as several small ones, are also clearly found in the $\bar{X}_i$ maps. So, we expect these local statistics with small $R$ values can be used to identify the point sources and foreground residuals, which will be discussed in a separate paper. If we choose $R = 5°$, from the middle panels in Figure 1 we find similar results, except for some non-Gaussianities in small point sources, which have been diluted for this case with larger $R$. In the right panels, we have chosen $R = 10°$, where the significant non-Gaussianities around the WMAP CS are clearly shown in all three maps.

Let us turn to the NILC5 map, which has a much higher resolution than ILC7. We first study the effect of different levels of smoothing. By adopting $R = 2°$, in Figure 2 we plot the $\bar{X}_i$ maps for $\theta_{\rm s} = 10'$ (left panels) and $\theta_{\rm s} = 40'$ (right panels). Interestingly enough for the case of lower smoothing, from the middle left and lower left panels we find a clear structure arising from $N_{\rm obs}$, i.e. the effective observations of WMAP for each pixel. We find a smaller $N_{\rm obs}$, which arises from a smaller pixel-noise variance, corresponds to a larger $\bar{X}_i^j$. So, these two local MF statistics can also be used to search for the morphology of the pixel-noise variance, which has been hidden in the temperature anisotropy map. We leave this as future work. Here, in order to reduce their effect, we should choose a larger smoothing parameter $\theta_{\rm s}$ as shown in the right panels in Figure 2, where we find the morphology of the pixel-noise variance disappears. However, the non-Gaussianity in the Galactic plane is still there, due to the heavy contamination caused by foreground residuals.

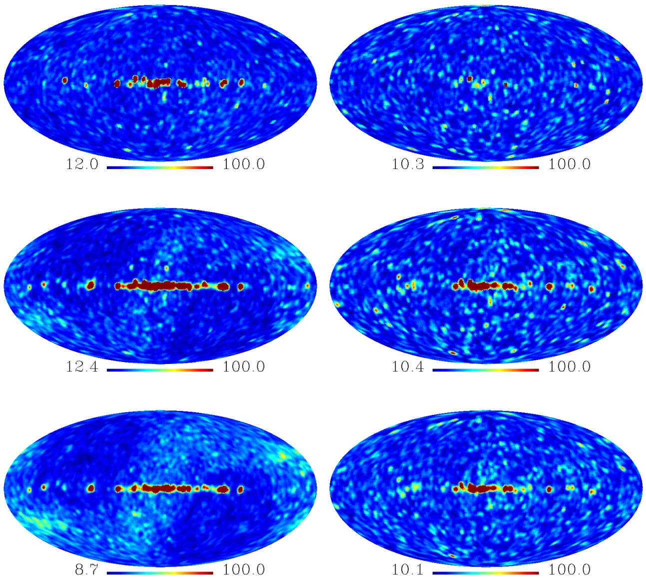


**Fig. 2** $\bar{X}_0(R)$ maps (*upper*), $\bar{X}_1(R)$ maps (*middle*) and $\bar{X}_2(R)$ maps (*lower*) from the NILC5 data with $R = 2^\circ$. In the left panels, the NILC5 map is smoothed by $\theta_\mathrm{s} = 10'$, and in the right panels, $\theta_\mathrm{s} = 40'$ smoothing is applied.

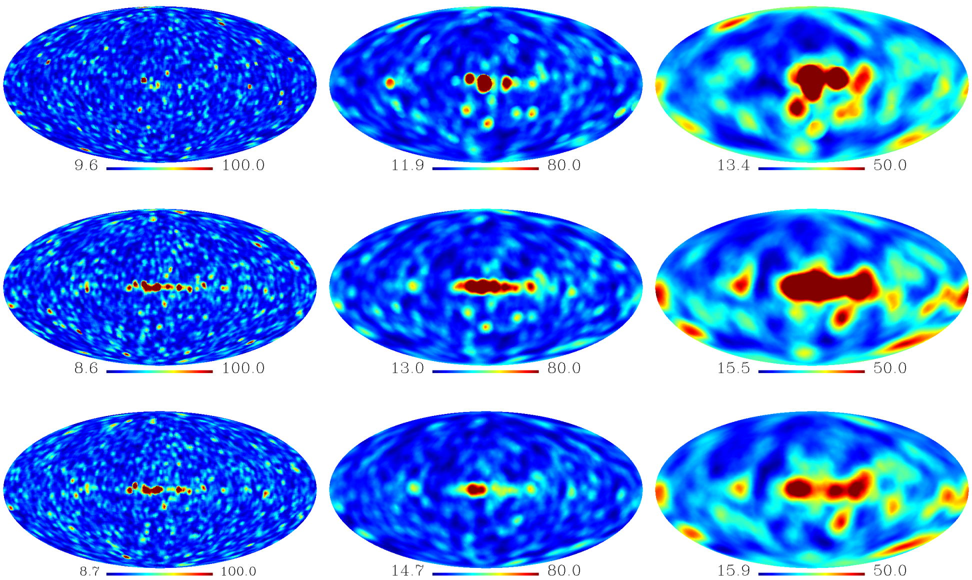


**Fig. 3** $\bar{X}_0(R)$ maps (*upper*), $\bar{X}_1(R)$ maps (*middle*) and $\bar{X}_2(R)$ maps (*lower*) from the NILC5 data with $\theta_\mathrm{s} = 60'$ smoothing. In the left panels we have used $R = 2^\circ$, in the middle panels $R = 5^\circ$ is chosen and in the right panel, $R = 10^\circ$.

Choosing a common smoothing parameter $\theta_s = 60'$, in Figure 3 we plot the $\bar{X}_i$ maps for $R = 2°$ (left), $R = 5°$ (middle) and $R = 10°$ (right). By comparing with those in Figure 1, we find that although several non-Gaussian point sources and foreground residuals in the Galactic plane are still there, NILC5 is much cleaner than ILC7, as claimed in Delabrouille et al. (2009). Meanwhile, we find that the non-Gaussianities around the WMAP CS are quite significant in the panels with $R = 10°$, which will be quantified in the next subsection.

### 3.3 Local Properties of the WMAP Cold Spot

Now, let us focus on the local properties of the WMAP CS by comparing with simulations that use Gaussian random distributions. Throughout this section, we only consider the maps which have been smoothed by $\theta_s = 60'$ to exclude the small-scale contaminations.

Firstly, we compare the WMAP CS with spots at the same position ($l = 209°, b = -57°$) in the random simulations. For a given $\bar{X}_i(R)$ map ($i = 0, 1, 2$) derived from WMAP data, the values of $\bar{X}_i(R)$ centered at the CS are calculated for the scales of $R = 2°, 3°, 4°, 5°, 6°, 7°, 8°, 9°, 10°, 11°$, $12°$, $13°$, $14°$and $15°$. The statistics for ILC7 maps are displayed in Figure 4. We compare them with 1000 Gaussian simulations. For each simulated sample, we select the spot at ($l = 209°$, $b = -57°$) and derive the corresponding $\bar{X}_i(R)$ maps. Then for each $i$ and $R$, we study the distribution of 1000 $\bar{X}_i(R)$ values, and construct confidence intervals for the statistics. The $68\%$, $95\%$ and $99\%$ confidence intervals are illustrated in Figure 4. From this figure, we find that for the $\bar{X}_0(R)$ statistics, the WMAP CS is consistent with the simulations. However, for the $\bar{X}_1(R)$ and $\bar{X}_2(R)$ statistics with $R > 6°$, the WMAP CS deviates from simulation at more than the $99\%$ confidence level. For the NILC5 case, we have also obtained similar results. These show that as anticipated, the WMAP CS is not a *normal spot*. The deviations at large scales imply that the WMAP CS seems to be a nontrivial large-scale structure, rather than a combination of some small non-Gaussian structures (for instance, point sources or foreground residuals, which always accompany non-Gaussianities at small scales), which is consistent with the conclusion in Zhao (2013).

Secondly, we compare the WMAP CS with the *coldest spots* in the Gaussian simulations. For every simulated map with $N_{\rm side} = 512$, we search for the *coldest spot* and derive the corresponding

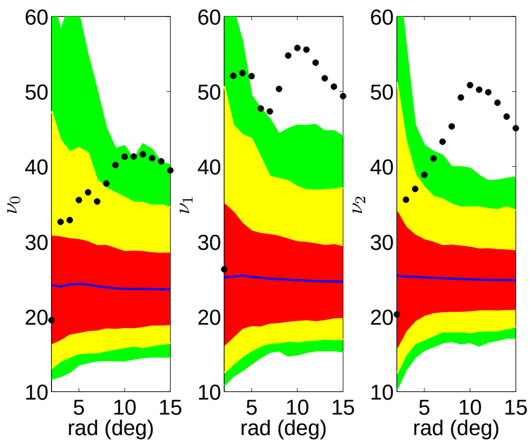


**Fig. 4** Three statistics for the spots at ($l = 209°$, $b = -57°$). Confidence regions obtained from 1000 Monte Carlo simulations are shown for $68\%$ (dark central region, *red online*), $95\%$ (lighter middle region, *yellow online*) and $99\%$ (lightest outer region, *green online*) levels, compared to the mean (*solid blue line*). The observed statistics for the WMAP ILC7 map are shown by solid dots (*black online*).

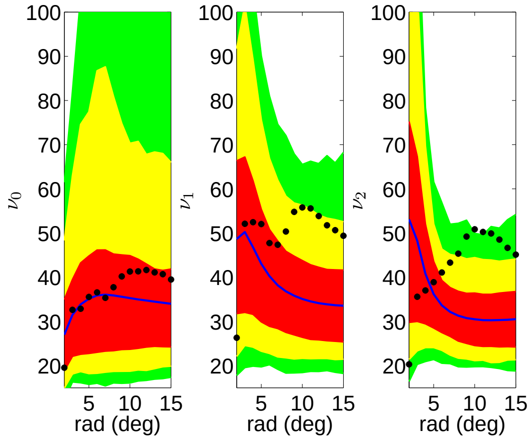


**Fig. 5** Three statistics for the *coldest spots*. Confidence regions obtained from 1000 Monte Carlo simulations are shown for 68% (dark central region, *red online*), 95% (lighter middle region, *yellow online*) and 99% (lightest outer region, *green online*) levels, compared to the mean (*solid blue line*). The observed statistics for the WMAP ILC7 map are shown by the solid dots (*black online*).

$\bar{X}_i(R)$ maps by the same calculations used for WMAP data. Then for each $i$ and $R$, we study the distribution of 1000 $\bar{X}_i(R)$ values, and construct confidence intervals for the statistics. The 68%, 95% and 99% confidence intervals are illustrated in Figure 5. We find that for the MF $\nu_0$, the WMAP CS is the *coldest spot* that follows a Gaussion distribution at all scales when comparing with simulations. For $\nu_1$ with $R > 7^\circ$, the WMAP CS only deviates from Gaussianity at the 68% confidence level. However, for the MF $\nu_2$ with $R > 7^\circ$, the deviation is quite significant (i.e. at more than the 95% level). In particular, for $\nu_2$ at the scale $R = 10^\circ \sim 11^\circ$, the deviations are more than at the 99% confidence level. Also, in the NILC5 case, similar deviations for these statistics have also been derived. So, we conclude that compared with the *coldest spots* in simulations, the WMAP CS significantly deviates from Gaussianity for MF $\nu_2$ at the scale $R \sim 10^\circ$. However, at smaller scales of $R < 6^\circ$, the deviations do not exist. These support that the WMAP CS seems to have a large-scale non-Gaussian structure.

In Cruz et al. (2007b, 2008), the authors found that the cosmic texture, rather than other explanations, provides an excellent interpretation for the WMAP CS, which has also been strongly supported by studying local departures from Gaussinity by temperature in terms of the mean, variance, skewness and kurtosis in our previous work (Zhao 2013). Here we shall test if local anomalies associated with the WMAP CS found in MFs are consistent with the interpretation using cosmic texture. The profile for the CMB temperature fluctuation caused by a collapsing cosmic texture is

$$\frac{\Delta T}{T} = \varepsilon / \sqrt{1 + 4\left(\frac{\vartheta}{\vartheta_c}\right)^2} \quad \text{for} \quad \vartheta \leq \vartheta_* \quad \text{and} \quad \frac{\Delta T}{T} = \frac{\varepsilon}{2} \mathrm{e}^{-\frac{1}{2\vartheta_c^2}(\vartheta^2 + \vartheta_*^2)} \quad \text{for} \quad \vartheta > \vartheta_*,$$

where $\vartheta$ is the angle from the center. $\varepsilon$ is the amplitude parameter and $\vartheta_c$ is the scale parameter. $\vartheta_* = \sqrt{3}/2\vartheta_c$. The best-fit texture parameters were obtained in Cruz et al. (2007b), $\varepsilon = -7.3 \times 10^{-5}$ and $\vartheta_c = 4.9^\circ$, which are adopted in our analysis. We subtract this cosmic texture structure from the ILC7 and NILC5 maps. Then, we repeat the analyses above by using these subtracted ILC maps. The corresponding results are presented in Figure 6 for ILC7 and Figure 7 for NILC5, where we find that the WMAP CS becomes quite normal, i.e. it becomes excellently consistent with *normal spots* in Gaussian simulations for any MF at any scale. So, we obtain the following conclusion: The

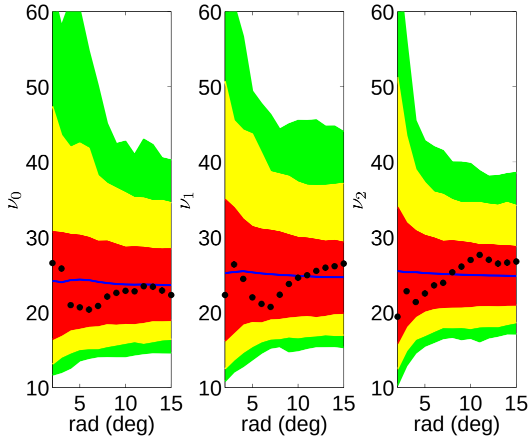


**Fig. 6** Same as Fig. 4, but here the cosmic texture structure has been subtracted from the WMAP ILC7 map.

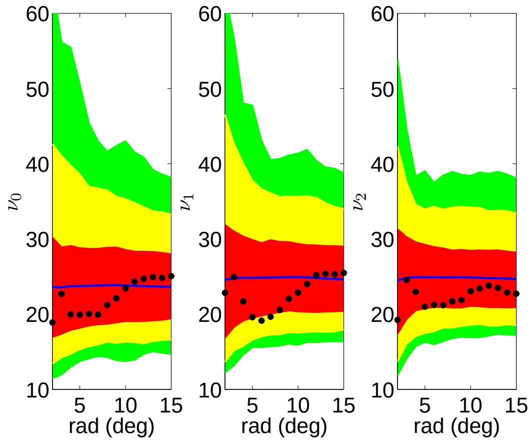


**Fig. 7** Same as Fig. 6, but here the WMAP ILC7 map is replaced by the NILC5 map.

local analysis of the WMAP CS by using local MF statistics strongly supports the explanation using cosmic texture.

## 4 CONCLUSIONS

Since the release of WMAP data, much attention has been paid to studying the non-Gaussian CS at Galactic coordinate ($l = 209°$, $b = -57°$), which might be produced by various small-scale contaminations, such as point sources or foregrounds, a supervoid in the Universe, or some phase transition in the early Universe. In this paper, in order to identify the WMAP CS and discriminate various explanations, we study the local properties of the CS by introducing the local MFs as related statistics. We find that compared with random Gaussian simulations, the WMAP CS definitely deviates from *normal spots* in simulations. In particular, it also deviates from the *coldest spots* in Gaussian samples at more than the 99% confidence level with a scale of $R \sim 10°$. All these support the fact that the WMAP CS is a large-scale non-Gaussian structure. Meanwhile, we find that the cosmic texture, which has a characteristic scale of about $10°$ and is claimed to be the most promising explanation of the CS by many authors, can excellently account for these anomalies in the local statistics. Hence, our analysis supports the explanation using cosmic texture for the WMAP CS.

**Acknowledgements** We appreciate useful discussions with P. Naselsky, J. Kim, M. Hansen and A.M. Frejsel. We acknowledge the use of the Legacy Archive for Microwave Background Data Analysis (LAMBDA). Our data analysis made use of HEALPix (Górski et al. 2005) and GLESP (Doroshkevich et al. 2005). This work is supported by the National Natural Science Foundation of China (Grant Nos. 11173021, 11075141 and 11322324) and the project of Knowledge Innovation Programme of CAS.

## References

Bennett, C. L., Hill, R. S., Hinshaw, G., et al. 2011, ApJS, 192, 17
Bernui, A., & Rebouças, M. J. 2009, Phys. Rev. D, 79, 063528
Bernui, A., & Rebouças, M. J. 2010, Phys. Rev. D, 81, 063533
Bernui, A., & Rebouças, M. J. 2012, Phys. Rev. D, 85, 023522
Cayón, L., Jin, J., & Treaster, A. 2005, MNRAS, 362, 826
Cruz, M., Martínez-González, E., Vielva, P., & Cayón, L. 2005, MNRAS, 356, 29
Cruz, M., Tucci, M., Martínez-González, E., & Vielva, P. 2006, MNRAS, 369, 57
Cruz, M., Cayón, L., Martínez-González, E., Vielva, P., & Jin, J. 2007a, ApJ, 655, 11
Cruz, M., Turok, N., Vielva, P., Martínez-González, E., & Hobson, M. 2007b, Science, 318, 1612
Cruz, M., Martínez-González, E., Vielva, P., et al. 2008, MNRAS, 390, 913
Delabrouille, J., Cardoso, J.-F., Le Jeune, M., et al. 2009, A&A, 493, 835
Doroshkevich, A. G., Naselsky, P. D., Verkhodanov, O. V., et al. 2005, International Journal of Modern Physics D, 14, 275
Eriksen, H. K., Novikov, D. I., Lilje, P. B., Banday, A. J., & Górski, K. M. 2004, ApJ, 612, 64
Górski, K. M., Hivon, E., Banday, A. J., et al. 2005, ApJ, 622, 759
Hikage, C., Komatsu, E., & Matsubara, T. 2006, ApJ, 653, 11
Hikage, C., Matsubara, T., Coles, P., et al. 2008, MNRAS, 389, 1439
Hikage, C., Koyama, K., Matsubara, T., Takahashi, T., & Yamaguchi, M. 2009, MNRAS, 398, 2188
Hikage, C., & Matsubara, T. 2012, MNRAS, 425, 2187
Inoue, K. T. 2012, MNRAS, 421, 2731
Inoue, K. T., & Silk, J. 2006, ApJ, 648, 23
Inoue, K. T., & Silk, J. 2007, ApJ, 664, 650
Komatsu, E., Dunkley, J., Nolta, M. R., et al. 2009, ApJS, 180, 330
Komatsu, E., Smith, K. M., Dunkley, J., et al. 2011, ApJS, 192, 18
Lim, E. A., & Simon, D. 2012, J. Cosmol. Astropart. Phys., 1, 048
Matsubara, T. 2010, Phys. Rev. D, 81, 083505
Naselsky, P. D., Christensen, P. R., Coles, P., et al. 2010, Astrophysical Bulletin, 65, 101
Novikov, D., Feldman, H. A., & Shandarin, S. F. 1999, International Journal of Modern Physics D, 8, 291
Planck Collaboration, Ade, P. A. R., Aghanim, N., et al. 2013, arXiv:1303.5083
Schmalzing, J., & Gorski, K. M. 1998, MNRAS, 297, 355
Tomita, H. 1986, Progress of Theoretical Physics, 76, 952
Vielva, P. 2010, Advances in Astronomy, 2010, 592094 (arXiv:1008.3051)
Vielva, P., Martínez-González, E., Barreiro, R. B., Sanz, J. L., & Cayón, L. 2004, ApJ, 609, 22
Winitzki, S., & Kosowsky, A. 1998, New Astron., 3, 75
Zhang, R., & Huterer, D. 2010, Astroparticle Physics, 33, 69
Zhao, W. 2013, MNRAS, 433, 3498